A first-principles self-consistent model of plasma turbulence and kinetic neutral dynamics in the tokamak scrape-off layer

2015 Nucl. Fusion 55 123014

(http://iopscience.iop.org/0029-5515/55/12/123014)

IOP Publishing | International Atomic Energy Agency Nuclear Fusion

Nucl. Fusion **55** (2015) 123014 (12pp) doi:10.1088/0029-5515/55/12/123014

A first-principles self-consistent model of plasma turbulence and kinetic neutral dynamics in the tokamak scrape-off layer

C. Wersal and P. Ricci

Ecole Polytechnique Fédérale de Lausanne (EPFL), Swiss Plasma Center (SPC), CH-1015 Lausanne, Switzerland

E-mail: christoph.wersal@epfl.ch

Received 12 May 2015, revised 23 September 2015
Accepted for publication 28 September 2015
Published 10 November 2015

Abstract

A first-principles self-consistent model that couples plasma and neutral physics suitable for the simulation of turbulent plasma behavior in the tokamak SOL is presented. While the plasma is modeled by the drift-reduced two fluid Braginskii equations, a kinetic model for the neutrals is developed, valid in short and in long mean free path scenarios. The model includes ionization, charge-exchange, recombination, and elastic collisional processes. The solution of the neutral kinetic equation is implemented within the GBS plasma turbulence code (Ricci *et al* 2012 *Plasma Phys. Control. Fusion* **54** 124047) and it is performed by using the method of characteristics. The details of the numerical implementation are discussed. Finally, we show initial results of the first self-consistent simulations of plasma turbulence and neutral dynamics.

Keywords: plasma physics, scrape-off layer, turbulence, kinetic neutral atoms, drift-reduced Braginskii

(Some figures may appear in colour only in the online journal)

1. Introduction

The first-principles understanding of the processes occurring in the tokamak scrape-off layer (SOL) remains an outstanding open issue in the way towards the construction of a fusion reactor. The SOL physics sets the boundary conditions for the plasma core, influencing the performance of the entire device, and it regulates the interaction of the plasma with the solid wall, determining the particle and power flux to the vessel. These have to stay within the material limits to prevent damage to the wall.

When ions and electrons outflowing from the SOL impact the solid walls, they recombine and they are re-emitted into the tokamak as neutral atoms and molecules that can penetrate into the SOL because of the low local plasma temperature. These recycled neutrals, which interact with the plasma through a number of collisional processes, play an important role in the SOL dynamics, and in regulating the heat and particle flux to the first wall.

To study the interplay between the neutral and the plasma dynamics in the SOL, plasma simulation codes based on phenomenological models for the turbulent transport are coupled to kinetic Monte Carlo codes that describe the behavior of the neutrals in the SOL (e.g. EIRENE [1], DEGAS 2 [2], NIMBUS [3], and others). The resulting codes (e.g. SOLEDGE2D-EIRENE [4], SOLPS, formerly B2-EIRENE, [5–7], EMC3-EIRENE [8], UEDGE [9], and others) remain the tool of reference for the design of tokamak divertors and they have been used for the ITER divertor [10]. On the other hand, the inclusion of the neutral dynamics in today's SOL codes that are derived from first-principles, i.e. that do not make use of empirical models or experimentally fitted parameters to describe SOL turbulence, is still in its infancy. In the two-dimensional turbulence simulation code TOKAM2D [11], the ionization of mono-energetic neutrals flying along the radial direction is self-consistently described within a plasma model that evolves plasma density and electric potential. Work with a two-dimensional fluid plasma and fluid neutral model has also

been recently reported [12]. Initial progress has been reported on the coupling of BOUT++ with EIRENE in linear geometry [13], and with a fluid neutral model[1].

In the present paper, we introduce a kinetic model for neutral atoms in the tokamak SOL, self-consistently evolved with the drift-reduced Braginskii equations [14] that describe the plasma dynamics in typical SOL conditions. The neutral kinetic model allows us to consider both short and long neutral mean free paths. We consider one mono-atomic neutral species, which is subject to four effective collision processes: charge-exchange (that includes elastic ion–neutral collisions), ionization, recombination, and elastic electron–neutral collisions. Although they may become important in detached scenario, we neglect neutral–neutral collisions, which have a lower reaction rate than charge-exchange and ionization processes in the typical attached SOL parameter regime. We note that additional neutral species can be included using the same model presented in this paper—this might become necessary to consider detachment conditions, or to include the details of the recycling from the main vessel wall.

The model is implemented and numerically solved within the GBS code [15], a three-dimensional numerical code developed to simulate SOL plasma turbulence. By solving the drift-reduced Braginskii equations, GBS evolves the full plasma profiles without separation of the plasma quantities into an equilibrium and fluctuating part, enabling the study of the self-consistent formation of the plasma profiles as the interplay of the plasma outflowing from the core, the parallel losses, and turbulent transport. GBS uses a proper set of boundary conditions at the presheath entrance [16], and it is able to treat electromagnetic perturbations [17].

This paper is structured as follows. After the Introduction, in section 2 we introduce the model for neutral atoms and the drift-reduced Braginskii equations suitable to describe plasma turbulence in the SOL and the interaction of the plasma with the neutrals. The method to solve the kinetic equation for neutrals is discussed in section 3. In section 4, first results of coupled plasma turbulence and neutral dynamics are presented. The conclusions and an outlook follow. The numerical implementation and the numerical convergence properties are added in the appendix.

2. The model

Here we present a model for the fusion fuel in the tokamak SOL that allows the first-principles self-consistent description of the plasma turbulent dynamics and the neutral physics. The model is composed of a kinetic model for the neutrals, which allows us to consider both long and short neutral mean free path scenarios, and a drift-reduced Braginskii model for the plasma that we deduce from the electron and ion kinetic equations. The boundary of the domain we consider is defined by the limiter or divertor plates, by the last closed flux surface (LCFS), and by a boundary surface facing the outer vessel wall.

2.1. The neutral model

We describe the dynamics of the distribution function of a single mono-atomic neutral species, f_n, by using the following kinetic equation

$$\frac{\partial f_n}{\partial t} + \boldsymbol{v}\cdot\frac{\partial f_n}{\partial \boldsymbol{x}} = -\nu_{iz} f_n - \nu_{cx}\left(f_n - \frac{n_n}{n_i} f_i\right) + \nu_{rec} f_i \quad (1)$$

being f_i, n_n, and n_i the ion distribution function, the neutral density, and the ion density, respectively. The ionization, charge-exchange, and recombination processes are described, respectively, through the use of Krook operators with collision frequencies defined as

$$\nu_{iz} = n_e\langle v_e \sigma_{iz}(v_e)\rangle \quad (2a)$$

$$\nu_{rec} = n_e\langle v_e \sigma_{rec}(v_e)\rangle \quad (2b)$$

$$\nu_{cx} = n_i\langle v_i \sigma_{cx}(v_i)\rangle \quad (2c)$$

where σ_{iz}, σ_{rec}, and σ_{cx} are the ionization, recombination, and charge-exchange cross sections, and v_e and v_i are the electron and ion velocities. The collisions frequencies, ν_{iz} and ν_{rec}, result from the averaging over the electron distribution function, neglecting therefore the neutral atom velocity, with respect to the electron one, in the evaluation of the relative velocity between the colliding particles. Regarding the charge-exchange collision frequency, ν_{cx}, we note that it depends weakly on the relative velocity between neutrals and ions [18], thus we neglect the neutral velocity in equation (2*c*) when evaluating the relative velocity of the colliding particles, and we average the cross section over the ion distribution function. The elastic electron–neutral collisions are neglected in the neutral equation, because of the electron to neutral mass ratio. In the present work, we use effective reaction rates for the $\langle v\sigma\rangle$ terms, which are taken from the OpenADAS[2] database, where they have been calculated using a collisional-radiative model [19].

We now describe the boundary conditions of equation (1). Being a kinetic advection equation, the boundary conditions for f_n have to be specified for the inward pointing velocities, that is for $\boldsymbol{v}$ such that $v_p = \boldsymbol{v}\cdot\hat{\boldsymbol{n}} > 0$, with $\hat{\boldsymbol{n}}$ the normal vector perpendicular to the boundary and pointing into the plasma region. At the limiter or divertor plates, the boundary of the domain over which equation (1) is solved coincides with the wall. We assume that the wall is saturated, i.e. that all impacting particles, neutrals and ions, are re-emitted from the wall instantly. A fraction of the particles impacting the wall, α_{refl}, is reflected, the rest is absorbed and released with a velocity that depends on the wall properties and that is independent of the impacting velocities. The parameter α_{refl}, which is assumed to be constant here, depends on the wall material and the SOL conditions (see, e.g. p 113 in [18]). The distribution function of the inflowing neutrals, $v_p > 0$, is therefore

$$f_n(\boldsymbol{x}_b, \boldsymbol{v}) = (1-\alpha_{refl})\Gamma_{out}(\boldsymbol{x}_b)\chi_{in}(\boldsymbol{x}_b, \boldsymbol{v}) + \alpha_{refl}[f_n(\boldsymbol{x}_b, \boldsymbol{v}-2\boldsymbol{v}_p) + f_i(\boldsymbol{x}_b, \boldsymbol{v}-2\boldsymbol{v}_p)], \quad (3)$$

[1] Dudson 2015 private communication.

[2] OpenADAS—http://open.adas.ac.uk

where $\boldsymbol{x}_\mathrm{b}$ is the vector position of a point on the boundary, specifically on the limiter or divertor plates in this case, and $\Gamma_\mathrm{out} = \int_{v_\mathrm{p}<0} |v_\mathrm{p}| f_\mathrm{n}\,\mathrm{d}v^3 + \Gamma_\mathrm{out,i}$ the flux of ions and neutrals outflowing towards the limiter or divertor plates. In particular, $\Gamma_\mathrm{out,i}$ is the outflowing perpendicular ion flux, and $\boldsymbol{v}_\mathrm{p} = v_\mathrm{p}\hat{\boldsymbol{n}}$ is the perpendicular neutral velocity with respect to the boundary. For the reflected part of the inflowing neutral distribution, we use spectral reflexion at the magnetic pre-sheath entrance, in particular, we neglect the acceleration of the ions in the sheath, and we assume unitary energy reflection coefficients (see, e.g. equation (3.2) in [18]). The inflowing velocity distribution, χ_in, is set according to the Knudsen Cosine law [20] to

$$\chi_\mathrm{in}(\boldsymbol{x}_\mathrm{b}, \boldsymbol{v}) = \frac{3}{4\pi}\frac{m^2}{T_\mathrm{b}^2}\cos(\theta)\exp\left(-\frac{mv^2}{2T_\mathrm{b}}\right) \tag{4}$$

being $\theta = \arccos(\hat{\boldsymbol{\Omega}}\cdot\hat{\boldsymbol{n}})$, $\hat{\boldsymbol{\Omega}} = \boldsymbol{v}/v$, and T_b the wall temperature. The function χ_in satisfies the property $\int_{v_\mathrm{p}>0} v_\mathrm{p}\chi_\mathrm{in}\mathrm{d}v^3 = 1$.

For the sake of simplicity, we place the outer boundary of the computational domain between the LCFS and the vessel wall, at a location where the plasma density drops to a negligible value. We remark that this boundary does not coincide with a physical surface. Particles that flow out through this boundary therefore travel towards the outer vessel wall, impact it, recycle, and then they re-enter the simulation domain. As particles can spread while moving towards the outer vessel wall and re-entering the domain, we evaluate the inflowing distribution function of the neutral atoms by using a local averaging procedure to redistribute the particles outflowing through the surface S that surrounds the position $\boldsymbol{x}_\mathrm{b}$ as

$$f_\mathrm{n}(\boldsymbol{x}_\mathrm{b}, \boldsymbol{v}) = \frac{\chi_\mathrm{in}(\boldsymbol{x}_\mathrm{b}, \boldsymbol{v})}{S}\int_S \Gamma_\mathrm{out}\mathrm{d}S \tag{5}$$

for $\boldsymbol{v}$ such that $v_\mathrm{p} > 0$. The surface S can depend on $\boldsymbol{x}_\mathrm{b}$.

At the LCFS, there are no neutral atoms flowing into the SOL, thus $f_\mathrm{n}(\boldsymbol{x}_\mathrm{b}, \boldsymbol{v}) = 0$ for $\boldsymbol{v}$ such that $v_\mathrm{p} > 0$. The integrated flux of neutral atoms outflowing from the SOL across the LCFS represents the source of density in the main tokamak plasma due to recycling.

2.2. The plasma model

For simplicity, we consider a single ion species plasma. We start our derivation of the drift-reduced Braginskii equations from the kinetic Boltzmann equation of ions and electrons, where we include collision terms in the form of Krook operators to describe the interaction with the neutrals. For the ion species we consider ionization, recombination, and charge-exchange processes, while for the electrons, we consider ionization, recombination, and elastic collision processes. Therefore, the kinetic equation for the ions is

$$\frac{\partial f_\mathrm{i}}{\partial t} + \boldsymbol{v}\cdot\frac{\partial f_\mathrm{i}}{\partial \boldsymbol{x}} + \boldsymbol{a}\cdot\frac{\partial f_\mathrm{i}}{\partial \boldsymbol{v}} = \nu_\mathrm{iz} f_\mathrm{n} - \nu_\mathrm{cx}\left(\frac{n_\mathrm{n}}{n_\mathrm{i}} f_\mathrm{i} - f_\mathrm{n}\right) - \nu_\mathrm{rec}\, f_\mathrm{i} + C(f_\mathrm{i}) \tag{6}$$

while the kinetic equation for the electrons is

$$\frac{\partial f_\mathrm{e}}{\partial t} + \boldsymbol{v}\cdot\frac{\partial f_\mathrm{e}}{\partial \boldsymbol{x}} + \boldsymbol{a}\cdot\frac{\partial f_\mathrm{e}}{\partial \boldsymbol{v}} = \nu_\mathrm{iz} n_\mathrm{n}\left[2\Phi_\mathrm{e}(\boldsymbol{v}_\mathrm{n}, T_\mathrm{e,iz}) - \frac{f_\mathrm{e}}{n_\mathrm{e}}\right] + \nu_\mathrm{en} n_\mathrm{n}\left[\Phi_\mathrm{e}(\boldsymbol{v}_\mathrm{n}, T_\mathrm{e,en}) - \frac{f_\mathrm{e}}{n_\mathrm{e}}\right] - \nu_\mathrm{rec} f_\mathrm{e} + C(f_\mathrm{e}) \tag{7}$$

where $\boldsymbol{a}$ is the particle acceleration due to the Lorentz force, $\Phi_\mathrm{e}(\boldsymbol{v}, T)$ is a Maxwellian distribution function for electrons, $C(f_\mathrm{i})$ and $C(f_\mathrm{e})$ are the Coulomb collision operators including both inter- and intra-species collisions for ions and electrons respectively, and the elastic electron–neutral collision frequency is $\nu_\mathrm{en} = n_\mathrm{e}\langle v_\mathrm{e}\sigma_\mathrm{en}(v_e)\rangle$.

While the interpretation of the collision terms in the ion kinetic equation is straightforward, as they correspond (with opposite sign) to those of the neutral equation (1), the collision operators in the electron kinetic equation deserve a longer discussion. When a neutral atom is ionized, the impacting fast electron is removed from the system, while two slower electrons appear. As a Krook collision term is used in equation (7), the loss rate of the fast electrons is proportional to the electron distribution function. Although it is not taken into account that the two resulting electrons might be emitted according to different distribution functions, the model can be reliably used to derive a fluid plasma description, as we do in the following. The two lower-energy electrons appear with a Maxwellian distribution function, $\Phi_\mathrm{e}(\boldsymbol{v}_\mathrm{n}, T_\mathrm{e,iz})$, of average velocity $\boldsymbol{v}_\mathrm{n} = \int \boldsymbol{v} f_\mathrm{n}\,\mathrm{d}\boldsymbol{v} / \int f_\mathrm{n}\,\mathrm{d}\boldsymbol{v}$ and temperature $T_\mathrm{e,iz} = T_\mathrm{e}/2 - E_\mathrm{iz}/3 + m_\mathrm{e}v_\mathrm{e}^2/6 - m_\mathrm{e}v_\mathrm{n}^2/3$, where T_e and v_e are the local electron temperature and fluid velocity respectively. This is deduced by assuming that the electrons are released isotropically in the neutral frame of reference, and that the total electron kinetic energy is reduced by the ionization energy, E_iz, when an ionization process occurs. We note that the ionization term in equation (7) takes into account the different paths to ionization (direct or through excited states), by using an effective ionization coefficient.

The electron–neutral collisions are modeled in equation (7) through a loss term proportional to the electron distribution function and a source with a Maxwellian distribution, $\Phi_\mathrm{e}(\boldsymbol{v}_\mathrm{n}, T_\mathrm{e,en})$. In fact, similarly to the ionization process, we impose that the electrons are scattered isotropically in the neutral frame of reference. Moreover, assuming that during the elastic electron–neutral collisions the electron kinetic energy is conserved during collisions with much heavier neutrals, one obtains $T_\mathrm{e,en} = T_\mathrm{e} + m_\mathrm{e}(v_\mathrm{e}^2 - v_\mathrm{n}^2)/3$. We note that the electron–neutral elastic collision term is neglected in the neutral kinetic equation (1), because of the small electron to neutral mass ratio.

Following the work of Braginskii [14], we now take the first three moments of the electron and ion kinetic equations in the limit $\omega_\mathrm{c}\tau \gg 1$, where $\omega_\mathrm{c} = qB/m$ is the gyro-frequency and τ the typical Coulomb collision time. In typical SOL conditions, the ion–neutral and electron–neutral collision time is much larger than the electron and ion Coulomb collision time, thus the presence of these collisions does not affect the closure

derived in [14]. In the case of high ion–neutral collisionality, $\omega_{ci}\tau_{i-n} \leqslant 1$, the closure terms have been derived by Helander *et al* in [21].

The Braginskii equations for the electron and ion densities, fluid velocities, and temperatures, derived in [14] including the additional plasma interaction terms with the neutrals are

$$\frac{\partial n_e}{\partial t} + \nabla \cdot (n_e \boldsymbol{v}_e) = n_n \nu_{iz} - n_i \nu_{rec} \tag{8a}$$

$$\frac{\partial n_i}{\partial t} + \nabla \cdot (n_i \boldsymbol{v}_i) = n_n \nu_{iz} - n_i \nu_{rec} \tag{8b}$$

$$m_e n_e \frac{\mathrm{d}_e v_{e\alpha}}{\mathrm{d}t} = -\frac{\partial p_e}{\partial x_\beta} - \frac{\partial \Pi_{e\alpha\beta}}{\partial x_\beta} - e n_e \left[E_\alpha + (\boldsymbol{v}_e \times \boldsymbol{B})_\alpha\right] + R_\alpha + m_e n_n (\nu_{en} + 2\nu_{iz})(v_{n\alpha} - v_{e\alpha}) \tag{8c}$$

$$m_i n_i \frac{\mathrm{d}_i v_{i\alpha}}{\mathrm{d}t} = -\frac{\partial p_i}{\partial x_\beta} - \frac{\partial \Pi_{i\alpha\beta}}{\partial x_\beta} + Z e n_i \left[E_\alpha + (\boldsymbol{v}_i \times \boldsymbol{B})_\alpha\right] - R_\alpha + m_i n_n (\nu_{iz} + \nu_{cx})(v_{n\alpha} - v_{i\alpha}) \tag{8d}$$

$$\frac{3}{2} n_e \frac{\mathrm{d}_e T_e}{\mathrm{d}t} + p_e \nabla \cdot \boldsymbol{v}_e = -\nabla \cdot \boldsymbol{q}_e - \Pi_{e\alpha\beta} \frac{\partial v_{e\alpha}}{\partial x_\beta} + Q_e + n_n \nu_{iz} \left[-E_{iz} - \frac{3}{2} T_e + \frac{3}{2} m_e \boldsymbol{v}_e \cdot \left(\boldsymbol{v}_e - \frac{4}{3} \boldsymbol{v}_n\right)\right] - n_n \nu_{en} m_e \boldsymbol{v}_e \cdot (\boldsymbol{v}_n - \boldsymbol{v}_e) \tag{8e}$$

$$\frac{3}{2} n_i \frac{\mathrm{d}_i T_i}{\mathrm{d}t} + p_i \nabla \cdot \boldsymbol{v}_i = -\nabla \cdot \boldsymbol{q}_i - \Pi_{i\alpha\beta} \frac{\partial v_{i\alpha}}{\partial x_\beta} + Q_i + n_n (\nu_{iz} + \nu_{cx}) \left[\frac{3}{2}(T_n - T_i) + \frac{m_i}{2}(\boldsymbol{v}_n - \boldsymbol{v}_i)^2\right] \tag{8f}$$

where $\Pi_{\alpha\beta}$ is the $\alpha\beta$ component of the stress tensor, $\boldsymbol{R}$ is the friction force between electrons and ions, p is the pressure, $\boldsymbol{q}$ is the heat flux density, Q is the heat generated by Coulomb collisions, Z is the ion charge, $\mathrm{d}_e/\mathrm{d}t = \partial/\partial t + (\boldsymbol{v}_e \cdot \nabla)$ and $\mathrm{d}_i/\mathrm{d}t = \partial/\partial t + (\boldsymbol{v}_i \cdot \nabla)$ are the electron and ion advective derivatives, and the subscripts e and i stand for electrons and the ion species respectively. The definitions of all fluid quantities can be found in the paper by Braginskii [14].

Despite their simplicity with respect to the kinetic equations, Braginskii's equations, equations (8), are not yet suitable to describe the plasma turbulence in the SOL. Therefore, we simplify the Braginskii equations in the drift limit, observing that $\mathrm{d}/\mathrm{d}t \ll \omega_{ci}$ for typical SOL turbulence. We follow the procedure described by, e.g. Zeiler [22]. In particular, to obtain the perpendicular ion velocity, we cross the ion momentum equation (8*d*), with $\boldsymbol{B}$, and rearrange the terms according to their order, writing $\boldsymbol{v}_{\perp i} = \boldsymbol{v}_{\perp i0} + \boldsymbol{v}_{i-n} + \boldsymbol{v}_{pol}$. The leading order term $\boldsymbol{v}_{\perp i0} = \boldsymbol{v}_E + \boldsymbol{v}_{di}$ is the sum of the $\boldsymbol{E} \times \boldsymbol{B}$ drift, $\boldsymbol{v}_E = (\boldsymbol{E} \times \boldsymbol{B})/B^2$, and the diamagnetic drift, $\boldsymbol{v}_{di} = (\boldsymbol{B} \times \nabla p_e)(enB^2)$, where we assume quasi-neutrality, $n_i = n_e = n$, and $Z = 1$. The drift arising from ion–neutral friction due to charge-exchange and elastic collisions, $\boldsymbol{v}_{i-n} = (\nu_{cx}/\omega_{ci})(\boldsymbol{v}_{\perp n} - \boldsymbol{v}_{\perp i}) \times \hat{\boldsymbol{b}}$, and the polarization drift, $\boldsymbol{v}_{pol}$, due to the ion inertia [22], are assumed to be of higher order in $(1/\omega_{ci})\mathrm{d}/\mathrm{d}t$ with respect to $\boldsymbol{v}_{\perp i0}$. While the ordering and the expression of $\boldsymbol{v}_{pol}$ have been discussed in detail by many authors (see, e.g. [22]), we notice that v_{i-n} is much smaller than the leading order term $v_{\perp i0}$, as $v_{i-n} \lesssim v_{\perp i}\nu_{cx}/\omega_{ci} \ll v_{\perp i0}$ in typical SOL conditions, where we assume that $v_{\perp n} \lesssim v_{\perp i}$. On the other hand, the terms proportional to m_e in the perpendicular electron velocity can be neglected leading to $\boldsymbol{v}_{\perp e} = \boldsymbol{v}_E + \boldsymbol{v}_{de}$, where $\boldsymbol{v}_{de} = (\boldsymbol{B} \times \nabla p_e)(enB^2)$.

The resulting drift-reduced Braginskii equations are

$$\frac{\partial n}{\partial t} = -\frac{1}{B}[\phi, n] - \nabla_\parallel (n v_{\parallel e}) + \frac{2}{eB}\left[C(p_e) - enC(\phi)\right] + \mathcal{D}_n(n) + S_n + n_n \nu_{iz} - n\nu_{rec} \tag{9a}$$

$$\frac{\partial \tilde{\omega}}{\partial t} = -\frac{1}{B}[\phi, \tilde{\omega}] - v_{\parallel i}\nabla_\parallel \tilde{\omega} + \frac{B^2}{m_i n}\nabla_\parallel j_\parallel + \frac{2B}{m_i n} C(p) + \mathcal{D}_{\tilde{\omega}}(\tilde{\omega}) - \frac{n_n}{n}\nu_{cx}\tilde{\omega} \tag{9b}$$

$$\frac{\partial v_{\parallel e}}{\partial t} + \frac{e}{m_e}\frac{\partial \Psi}{\partial t} = -\frac{1}{B}[\phi, v_{\parallel e}] - v_{\parallel e}\nabla_\parallel v_{\parallel e} + \frac{e}{\sigma_\parallel m_e} j_\parallel + \frac{e}{m_e}\nabla_\parallel \phi - \frac{T_e}{m_e n}\nabla_\parallel n - \frac{1.71}{m_e}\nabla_\parallel T_e + \mathcal{D}_{v_{\parallel e}}(v_{\parallel e}) + \frac{n_n}{n}(\nu_{en} + 2\nu_{iz})(v_{\parallel n} - v_{\parallel e}) \tag{9c}$$

$$\frac{\partial v_{\parallel i}}{\partial t} = -\frac{1}{B}[\phi, v_{\parallel i}] - v_{\parallel i}\nabla_\parallel v_{\parallel i} - \frac{1}{m_i n}\nabla_\parallel p + \mathcal{D}_{v_{\parallel i}}(v_{\parallel i}) + \frac{n_n}{n}(\nu_{iz} + \nu_{cx})(v_{\parallel n} - v_{\parallel i}) \tag{9d}$$

$$\frac{\partial T_e}{\partial t} = -\frac{1}{B}[\phi, T_e] - v_{\parallel e}\nabla_\parallel T_e + \frac{4T_e}{3eB}\left[\frac{T_e}{n}C(n) + \frac{7}{2}C(T_e) - eC(\phi)\right] + \frac{2T_e}{3n}\left[\frac{0.71}{e}\nabla_\parallel j_\parallel - n\nabla_\parallel v_{\parallel e}\right] + \mathcal{D}_{T_e}(T_e) + \mathcal{D}^\parallel_{T_e}(T_e) + S_{T_e} + \frac{n_n}{n}\nu_{iz}\left[-\frac{2}{3}E_{iz} - T_e + m_e v_{\parallel e}\left(v_{\parallel e} - \frac{4}{3}v_{\parallel n}\right)\right] - \frac{n_n}{n}\nu_{en} m_e \frac{2}{3} v_{\parallel e}(v_{\parallel n} - v_{\parallel e}) \tag{9e}$$

$$\frac{\partial T_i}{\partial t} = -\frac{1}{B}[\phi, T_i] - v_{\parallel i}\nabla_\parallel T_i + \frac{4T_i}{3eB}\left[C(T_e) + \frac{T_e}{n}C(n) - \frac{5}{2}C(T_i) - eC(\phi)\right] + \frac{2T_i}{3n}\left[\frac{1}{e}\nabla_\parallel j_\parallel - n\nabla_\parallel v_{\parallel i}\right] + \mathcal{D}_{T_i}(T_i) + \mathcal{D}^\parallel_{T_i}(T_i) + S_{T_i} + \frac{n_n}{n}(\nu_{iz} + \nu_{cx})\left[T_n - T_i + \frac{1}{3}(v_{\parallel n} - v_{\parallel i})^2\right] \tag{9f}$$

with $p = n(T_e + T_i)$, the total pressure, and $\sigma_\parallel = 1.96 e^2 n \tau_e / m_e$, the parallel conductivity, where τ_e is the electron collision time. The generalized vorticity, $\tilde{\omega} = \omega + 1/e\nabla^2_\perp T_i$, is related to the electrostatic potential by $\nabla^2_\perp \phi = \omega$, while $(\beta_{e0}/2)\nabla^2_\perp \Psi = j_\parallel$, with $\beta_{e0} = 2\mu_0 p_e/B^2$. The following operators have been introduced $\nabla_\parallel A = \hat{\boldsymbol{b}} \cdot \nabla A + \hat{\boldsymbol{b}}/B \times \nabla_\perp \Psi \cdot \nabla A$, $\quad [A, B] = \hat{\boldsymbol{b}} \cdot (\nabla A \times \nabla B)$, and $C(A) = B/2[\nabla \times (\hat{\boldsymbol{b}}/B)] \cdot \nabla A$.

We note that the density equation (9*a*) is derived from the electron density equation (8*a*), and that the vorticity equation (9*b*), is obtained by subtracting equation (8*a*) from equation (8*b*), applying quasi-neutrality, $n_\mathrm{i} = n_\mathrm{e} = n$, and using the Boussinesq-approximation. The term resulting from the ion–neutral friction drift in equation (9*b*) has been evaluated by approximating $\boldsymbol{v}_{\mathrm{i}-\mathrm{n}} \simeq (\nu_{\mathrm{cx}}/\omega_{\mathrm{ci}})(\boldsymbol{v}_{\perp\mathrm{n}} - \boldsymbol{v}_{\perp\mathrm{i}0}) \times \hat{\boldsymbol{b}}$ and assuming $\nabla \cdot \boldsymbol{v}_{\perp\mathrm{n}} \ll \nabla \cdot \boldsymbol{v}_{\perp\mathrm{i}0}$, which is true for $\rho_{\mathrm{s}0}/\lambda_{\mathrm{mfp,n}} \ll 1$. ($\rho_{\mathrm{s}0} = c_{\mathrm{s}0}/\Omega_{\mathrm{ci}}$ is the ion sound Larmor radius, $c_{\mathrm{s}0} = \sqrt{T_{\mathrm{e}0}/m_\mathrm{i}}$ is the plasma sound speed, $T_{\mathrm{e}0}$ is the electron temperature at the LCFS, and $\lambda_{\mathrm{mfp,n}}$ is the mean free path of the neutrals.) The contribution of the electron–neutral friction drift in the vorticity equation (9*b*), has been neglected due to the small electron to ion mass ratio. We remark that we neglect $\boldsymbol{v}_{\mathrm{pol}}$ and $\boldsymbol{v}_{\mathrm{i}-\mathrm{n}}$ in the advective derivative $\mathrm{d}/\mathrm{d}t$.

The boundary conditions at the magnetic presheath entrance of the limiter plates for the drift-reduced Braginskii equations are discussed in [16], where a set of first-principles boundary conditions was derived. We remark that the boundary conditions of the kinetic neutral equation (1), at the limiter or divertor plates, equation (3), are specified directly at the solid wall, and not at the magnetic presheath entrance. However, since the neutral mean free path is typically much longer than the width of the magnetic presheath, we will assume that the boundary of the neutral kinetic equation coincides with the magnetic presheath entrance.

We remark that equations (9), in the limit of $n_\mathrm{n} \to 0$, have been implemented in the GBS code [15] and used in the past to study the main properties of plasma turbulence in the tokamak SOL. Investigations carried out with GBS have significantly advanced our understanding of, e.g. the turbulent saturation mechanisms in the SOL [23], the SOL turbulent regimes [24], the phenomena behind the generation of intrinsic rotation [25], the scaling of the SOL width in inner-wall limited tokamak plasma [26], and the equilibrium electrostatic potential [27].

3. Formal solution of the neutral kinetic equation in typical SOL relevant parameters

We now solve the kinetic advection equation for the neutrals, equation (1), by using the method of characteristics, under the assumption that plasma-related quantities are known. The formal solution of equation (1) is

$$f_\mathrm{n}(\boldsymbol{x},\boldsymbol{v},t) = \int_0^{r'_\mathrm{b}} \left[\frac{S(\boldsymbol{x}',\boldsymbol{v},t')}{v} + \delta(r'-r'_\mathrm{b}) f_\mathrm{n}(\boldsymbol{x}'_\mathrm{b},\boldsymbol{v},t'_\mathrm{b})\right] \times \exp\left[-\frac{1}{v}\int_0^{r'} \nu_{\mathrm{eff}}(\boldsymbol{x}'',t'')\mathrm{d}r''\right]\mathrm{d}r' \qquad (10)$$

where $\boldsymbol{x}' = \boldsymbol{x} - r'\hat{\boldsymbol{\Omega}}$, $t' = t - r'/v$, and $\hat{\boldsymbol{\Omega}} = \boldsymbol{v}/v$. (The single prime is used to indicate the source location of neutrals.) Similar definitions apply to $\boldsymbol{x}''$ and t''. (The double prime is used for locations along the path integral between the source, $\boldsymbol{x}'$, and target location, $\boldsymbol{x}$.) Moreover, the subscript b is used as an indication for a position on the boundary. Therefore, $\boldsymbol{x}'_\mathrm{b} = \boldsymbol{x} - r'_\mathrm{b}\hat{\boldsymbol{\Omega}}$ is the intersection of the vector parallel to $\hat{\boldsymbol{\Omega}}$, starting at $\boldsymbol{x}$, with the boundary, and $t'_\mathrm{b} = t - r'_\mathrm{b}/v$. The neutral source term consists of a volumetric source, $S(\boldsymbol{x}',\boldsymbol{v},t')$, resulting from charge-exchange and recombination processes, given by

$$S(\boldsymbol{x}',\boldsymbol{v},t') = \nu_{\mathrm{cx}}(\boldsymbol{x}',t')n_\mathrm{n}(\boldsymbol{x}',t')\Phi_\mathrm{i}(\boldsymbol{x}',\boldsymbol{v},t') + \nu_{\mathrm{rec}}(\boldsymbol{x}',t')f_\mathrm{i}(\boldsymbol{x}',\boldsymbol{v},t'), \qquad (11)$$

and the term $\delta(r'-r'_\mathrm{b})f_\mathrm{n}(\boldsymbol{x}'_\mathrm{b},\boldsymbol{v},t'_\mathrm{b})$, localized at the boundary of the domain, where $f_\mathrm{n}(\boldsymbol{x}'_\mathrm{b},\boldsymbol{v},t'_\mathrm{b})$ is given by the boundary conditions, equations (3) and (5). The effective cross-section for the removal of the neutrals is given by $\nu_{\mathrm{eff}}(\boldsymbol{x}'',t'') = \nu_{\mathrm{iz}}(\boldsymbol{x}'',t'') + \nu_{\mathrm{cx}}(\boldsymbol{x}'',t'')$. Because $S(\boldsymbol{x}',\boldsymbol{v},t')$ depends on $n_\mathrm{n}(\boldsymbol{x}',t') = \int f_\mathrm{n}(\boldsymbol{x}',\boldsymbol{v},t')\mathrm{d}\boldsymbol{v}$ (see equation (11)), equation (10) is an integral equation for f_n in the spatial and velocity domain that involves plasma and neutral quantities at past times.

We now consider two approximations, valid in the typical SOL parameter regime, which considerably simplify equation (10) and therefore the numerical investigation of the neutral dynamics. First, we Taylor expand the source term S and the other time-dependent quantities appearing in the integral in equation (10) about time $t' = t$, i.e.

$$S(\boldsymbol{x}',t') = S\left(\boldsymbol{x}',t-\frac{r'}{v}\right) = S(\boldsymbol{x}',t) - \left.\frac{\partial S(\boldsymbol{x}',t')}{\partial t'}\right|_{t'=t}\frac{r'}{v} + o\left(\frac{r'}{v}\right). \qquad (12)$$

We now note that S varies in time on the typical plasma turbulent time scale, τ_{turb}, while r'/v constitutes the typical flight time of the neutrals, τ_n, which can be estimated as $\tau_\mathrm{n} \sim \nu_{\mathrm{eff}}^{-1}$. For typical SOL parameters $\tau_\mathrm{n} < \tau_{\mathrm{turb}}$. It follows therefore that we can approximate $S(\boldsymbol{x}',t') \simeq S(\boldsymbol{x}',t)$, which corresponds to taking $\partial_t f_\mathrm{n} = 0$ in equation (1). This has been denoted as the neutral adiabatic regime [28].

Second, we take advantage of the plasma turbulence anisotropy to reduce the solution of the three-dimensional neutral model to a set of two-dimensional problems. In fact, turbulent plasma structures are considerably more elongated along the magnetic field lines than perpendicular to them, $k_\parallel \ll k_\perp$, and the neutral mean free path, $\lambda_{\mathrm{mfp,n}}$, is typically much shorter (of the order of millimeters or centimeters) than the parallel elongation of the turbulent plasma structures, which is of the order of the machine size (i.e. of the order of a meter). We therefore have $\lambda_{\mathrm{mfp,n}} \sim v/\nu_{\mathrm{eff}} \ll 1/k_\parallel$. (We remark that neutrals in the tail of the distribution function originating from charge exchange processes might have much longer mean free paths, but $\lambda_{\mathrm{mfp,n}} \ll 1/k_\parallel$ is fulfilled for the bulk of the neutrals in a typical tokamak SOL.) To take advantage of the plasma anisotropy, we introduce a set of coordinates aligned to $\boldsymbol{B}$, that is $\boldsymbol{x} = (\boldsymbol{x}_\perp, x_\parallel)$, where $\boldsymbol{x}_\perp$ denotes the coordinates in the direction perpendicular to $\boldsymbol{B}$, and $x_\parallel$ parallel to it. We note that $x_\parallel$ approximately coincides with the toroidal direction, and $\boldsymbol{x}_\perp$ denotes the coordinate in the poloidal plane, in the large aspect ratio limit and at the large value of the safety factor of typical tokamak SOL ($R/a \gg 1$, $q > 1$). We expand the source S and the other quantities appearing in equation (10) about $x'_\parallel = x_\parallel$, that is

$$S(\boldsymbol{x}'_\perp, x'_\parallel, t) = S(\boldsymbol{x}'_\perp, x_\parallel, t) + \left.\frac{\partial S(\boldsymbol{x}'_\perp, x'_\parallel, t)}{\partial x'_\parallel}\right|_{x'_\parallel = x_\parallel} (x'_\parallel - x_\parallel) + o(x'_\parallel - x_\parallel). \quad (13)$$

Now, because of the exponential decay due to ionization and charge exchange processes, the contribution of S to the integral in equation (10) becomes small at distances longer than $\lambda_{\mathrm{mfp,n}}$. Therefore, the expansion in equation (13) has to be considered for $x'_\parallel - x_\parallel \lesssim \lambda_{\mathrm{mfp,n}}$. Being $\partial_{x'_\parallel} S(\boldsymbol{x}'_\perp, x'_\parallel, t) \sim k_\parallel S(\boldsymbol{x}'_\perp, x'_\parallel, t)$, and $k_\parallel \lambda_{\mathrm{mfp,n}} \ll 1$, it follows that $S(\boldsymbol{x}'_\perp, x'_\parallel, t) \simeq S(\boldsymbol{x}'_\perp, x_\parallel, t)$ in the regime of interest.

Within the adiabatic approximation and the assumption of $k_\parallel \lambda_{\mathrm{mfp,n}} \ll 1$ the formal solution of the neutral kinetic equation (1), becomes

$$f_{\mathrm{n}}(\boldsymbol{x}_\perp, x_\parallel, \boldsymbol{v}, t) = \int_0^{r_{\perp\mathrm{b}}} \left[\frac{S(\boldsymbol{x}'_\perp, x_\parallel, \boldsymbol{v}, t)}{v_\perp} + \delta(r'_\perp - r_{\perp\mathrm{b}}) f_{\mathrm{n}}(\boldsymbol{x}'_{\perp b}, x_\parallel, \boldsymbol{v}, t)\right] \times \exp\left[-\frac{1}{v_\perp}\int_0^{r'_\perp} \nu_{\mathrm{eff}}(\boldsymbol{x}''_\perp, x_\parallel, t)\mathrm{d}r''_\perp\right]\mathrm{d}r'_\perp \quad (14)$$

where $r'_\perp$ has been defined through $\boldsymbol{x}'_\perp = \boldsymbol{x}_\perp - r'_\perp \hat{\boldsymbol{\Omega}}_\perp, \hat{\boldsymbol{\Omega}}_\perp = \boldsymbol{v}_\perp / v_\perp$, and $\boldsymbol{v}_\perp$ is the perpendicular velocity. Since the dependencies in equation (14) on the parallel direction and on time are parametric, in the following, for better readability, we do not carry over the explicit notation of the t and $x_\parallel$ dependence.

In equation (14), the recombination term contained in S [see equation (11)], as well as the term associated to ion recycling at the limiter present in the boundary conditions, do not depend on $f_{\mathrm{n}}(\boldsymbol{x}_\perp, \boldsymbol{v})$ and can be evaluated once the plasma quantities are known. On the other hand, the charge-exchange collision term on the right-hand side of equation (14) contained in S, and the reflected or re-emitted neutrals from the walls, which appear in the boundary term, depend on $f_{\mathrm{n}}(\boldsymbol{x}_\perp, \boldsymbol{v})$ through $n_{\mathrm{n}}(\boldsymbol{x}_\perp)$. This suggests that a linear integral equation for $n_{\mathrm{n}}(\boldsymbol{x}_\perp)$ can be obtained by integrating equation (14) in velocity space, which is

$$n_{\mathrm{n}}(\boldsymbol{x}_\perp) = \int_0^\infty \mathrm{d}v_\perp v_\perp \int_0^{2\pi} \mathrm{d}\vartheta \int_{-\infty}^\infty \mathrm{d}v_\parallel \int_0^{r_{\perp\mathrm{b}}} \mathrm{d}r'_\perp \times\left\{\left[\frac{S(\boldsymbol{x}'_\perp, \boldsymbol{v})}{v_\perp} + \delta(r'_\perp - r'_{\perp\mathrm{b}}) f_{\mathrm{n}}(\boldsymbol{x}'_\perp, \boldsymbol{v})\right] \times \exp\left[-\frac{1}{v_\perp}\int_0^{r'_\perp} \nu_{\mathrm{eff}}(\boldsymbol{x}''_\perp)\mathrm{d}r''_\perp\right]\right\} \quad (15)$$

where we use cylindrical coordinates, $(v_\perp, \vartheta, v_\parallel)$, in velocity space (also in this case parallel and perpendicular denote the direction with respect to the magnetic field).

We now describe two properties that help us simplify equation (15). First, for a generic function $F(\boldsymbol{x}_\perp, \boldsymbol{x}'_\perp)$ we can write

$$\int_0^{r_{\perp\mathrm{b}}} \mathrm{d}r'_\perp \int_0^{2\pi} \mathrm{d}\vartheta F(\boldsymbol{x}_\perp, \boldsymbol{x}'_\perp) = \int_D \mathrm{d}A' \frac{1}{r'_\perp} F(\boldsymbol{x}_\perp, \boldsymbol{x}'_\perp), \quad (16)$$

where $\mathrm{d}A'$ is the infinitesimal area of D, which is the part of the plane perpendicular to the magnetic field, approximatively corresponding to the poloidal plane, that is optically connected to $\boldsymbol{x}_\perp$. Second, we use the following property,

$$\int_0^{r_{\perp\mathrm{b}}} \mathrm{d}r'_\perp \int_0^{2\pi} \mathrm{d}\vartheta \delta(r'_\perp - r'_{\perp\mathrm{b}}) F(\boldsymbol{x}_\perp, \boldsymbol{x}'_\perp) = \int_{\partial D} \mathrm{d}a'_{\mathrm{b}} \frac{\cos\theta'}{r'_{\perp\mathrm{b}}} F(\boldsymbol{x}_\perp, \boldsymbol{x}'_{\perp\mathrm{b}}), \quad (17)$$

where $\mathrm{d}a'_{\mathrm{b}}$ is the infinitesimal length along ∂D, which is the boundary of D, and $\theta' = \arccos\,|\hat{\boldsymbol{\Omega}}_\perp \cdot \hat{\boldsymbol{n}}|$ is the angle between $\hat{\boldsymbol{\Omega}}_\perp$ and $\hat{\boldsymbol{n}}$ at the boundary location, $\boldsymbol{x}'_{\perp\mathrm{b}}$. In fact, the r' integral gives

$$\int_0^{r_{\perp\mathrm{b}}} \mathrm{d}r'_\perp \int_0^{2\pi} \mathrm{d}\vartheta \delta(r'_\perp - r'_{\perp\mathrm{b}}) F(\boldsymbol{x}_\perp, \boldsymbol{x}'_\perp) = \int_0^{2\pi} \mathrm{d}\vartheta F(\boldsymbol{x}_\perp, \boldsymbol{x}'_{\perp\mathrm{b}}), \quad (18)$$

and the ϑ integral is transformed to a line integral along ∂D by using the law of sines for the triangle in figure 1, namely

$$\frac{\mathrm{d}a'_{\mathrm{b}}}{\mathrm{d}\vartheta} = \frac{r'_{\perp\mathrm{b}}}{\sin(\alpha)} = \frac{r'_{\perp\mathrm{b}}}{\cos(\theta')}, \quad (19)$$

as $\alpha = \pi/2 - \theta'$ for infinitesimal small $\mathrm{d}\vartheta$.

Now, by rearranging the integrals in equation (15) and using the two properties, equations (16) and (17), we obtain

$$\begin{aligned} n_{\mathrm{n}}(\boldsymbol{x}_\perp) = {} & \int_D \mathrm{d}A' \frac{1}{r'_\perp} \int_0^\infty \mathrm{d}v_\perp v_\perp \\ & \times \int_{-\infty}^\infty \mathrm{d}v_\parallel \left\{\frac{S(\boldsymbol{x}'_\perp, \boldsymbol{v})}{v_\perp} \exp\left[-\frac{1}{v_\perp}\int_0^{r'_\perp} \nu_{\mathrm{eff}}(\boldsymbol{x}''_\perp)\mathrm{d}r''_\perp\right]\right\} \\ & + \int_{\partial D} \mathrm{d}a'_{\mathrm{b}} \frac{\cos\theta'}{r'_{\perp\mathrm{b}}} \int_0^\infty \mathrm{d}v_\perp v_\perp \\ & \times \int_{-\infty}^\infty \mathrm{d}v_\parallel \left\{f_{\mathrm{n}}(\boldsymbol{x}'_{\perp\mathrm{b}}, \boldsymbol{v}) \exp\left[-\frac{1}{v_\perp}\int_0^{r'_{\perp\mathrm{b}}} \nu_{\mathrm{eff}}(\boldsymbol{x}''_\perp)\mathrm{d}r''_\perp\right]\right\}. \end{aligned} \quad (20)$$

The quantities that do not depend on velocity, that is $n_{\mathrm{n}}(\boldsymbol{x}'_\perp)$, $\nu_{\mathrm{cx}}(\boldsymbol{x}'_\perp)$, and $\Gamma_{\mathrm{out}}(\boldsymbol{x}'_{\perp\mathrm{b}})$ [inside $S(\boldsymbol{x}'_\perp, \boldsymbol{v})$, and $f_{\mathrm{n}}(\boldsymbol{x}'_{\perp\mathrm{b}}, \boldsymbol{v})$ respectively], can be taken out of the velocity integrals, leading to an integral equation for $n_{\mathrm{n}}(\boldsymbol{x}_\perp)$, which is

$$\begin{aligned} n_{\mathrm{n}}(\boldsymbol{x}_\perp) = {} & \int_D n_{\mathrm{n}}(\boldsymbol{x}'_\perp) \nu_{\mathrm{cx}}(\boldsymbol{x}'_\perp) K_{\mathrm{p}\to\mathrm{p}}(\boldsymbol{x}_\perp, \boldsymbol{x}'_\perp) \mathrm{d}A' \\ & + \int_{\partial D} \Gamma_{\mathrm{out}}(\boldsymbol{x}'_{\perp\mathrm{b}}) K_{\mathrm{b}\to\mathrm{p}}(\boldsymbol{x}_\perp, \boldsymbol{x}'_{\perp\mathrm{b}}) \mathrm{d}a'_{\mathrm{b}} + n_{\mathrm{n,rec}}(\boldsymbol{x}_\perp), \end{aligned} \quad (21)$$

where Γ_{out}, the perpendicular component of neutral and ion flux outflowing into the boundary, is

$$\Gamma_{\mathrm{out}}(\boldsymbol{x}_{\perp\mathrm{b}}) = \int v_\perp \cos\theta f_{\mathrm{n}}(\boldsymbol{x}_{\perp\mathrm{b}}, \boldsymbol{v}_\perp) \mathrm{d}\boldsymbol{v}_\perp + \Gamma_{\mathrm{out,i}}(\boldsymbol{x}_{\perp\mathrm{b}}) \quad (22)$$

$$\begin{aligned} = {} & \int_D n_{\mathrm{n}}(\boldsymbol{x}'_\perp) \nu_{\mathrm{cx}}(\boldsymbol{x}'_\perp) K_{\mathrm{p}\to\mathrm{b}}(\boldsymbol{x}_{\perp\mathrm{b}}, \boldsymbol{x}'_\perp) \mathrm{d}A' \\ & + \int_{\partial D} \Gamma_{\mathrm{out}}(\boldsymbol{x}'_{\perp\mathrm{b}}) K_{\mathrm{b}\to\mathrm{b}}(\boldsymbol{x}_{\perp\mathrm{b}}, \boldsymbol{x}'_{\perp\mathrm{b}}) \mathrm{d}a'_{\mathrm{b}} \\ & + \Gamma_{\mathrm{out,rec}}(\boldsymbol{x}_{\perp\mathrm{b}}) + \Gamma_{\mathrm{out,i}}(\boldsymbol{x}_{\perp\mathrm{b}}), \end{aligned} \quad (23)$$

and where $\theta = \arccos\,|\hat{\boldsymbol{\Omega}}_\perp \cdot \hat{\boldsymbol{n}}|$ is the angle between $\hat{\boldsymbol{\Omega}}_\perp$ and $\hat{\boldsymbol{n}}$ at the target location, $\boldsymbol{x}_{\perp\mathrm{b}}$. Moreover, the following kernel functions have been defined

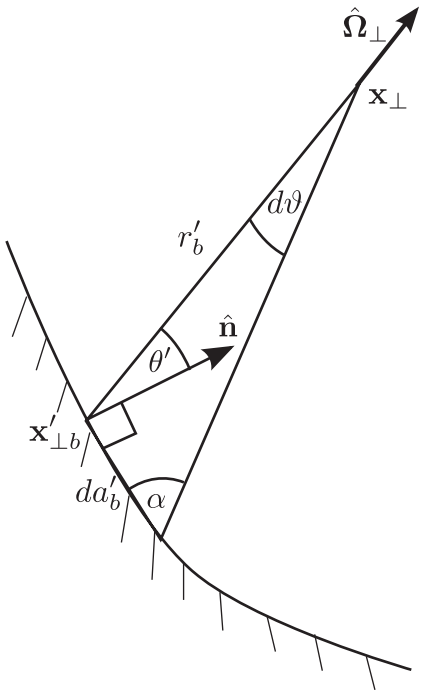

Figure 1. Illustration of the transformation from an angular integral (in ϑ) to a line integral (in a'_b) for neutrals coming from a section of the boundary of length $\mathrm{d}a'_\mathrm{b}$ at $\boldsymbol{x}'_{\perp\mathrm{b}}$ arriving at $\boldsymbol{x}_\perp$ flying in the direction $\hat{\boldsymbol{\Omega}}_\perp$.

$$K_{\mathrm{p}\to\mathrm{p}}(\boldsymbol{x}_\perp,\boldsymbol{x}'_\perp)=\int_0^\infty \frac{1}{r'_\perp}\Phi_{\perp\mathrm{i}}(\boldsymbol{x}'_\perp,\boldsymbol{v}_\perp)\exp\left[-\frac{1}{v_\perp}\int_0^{r'_\perp}\nu_{\mathrm{eff}}(\boldsymbol{x}''_\perp)\mathrm{d}r''_\perp\right]\mathrm{d}v_\perp \tag{24a}$$

$$K_{\mathrm{b}\to\mathrm{p}}(\boldsymbol{x}_\perp,\boldsymbol{x}'_{\perp\mathrm{b}})=\int_0^\infty \frac{v_\perp}{r'_\perp}\cos\theta'\chi_{\perp\mathrm{in}}(\boldsymbol{x}'_{\perp\mathrm{b}},\boldsymbol{v}_\perp)\times\exp\left[-\frac{1}{v_\perp}\int_0^{r'_\perp}\nu_{\mathrm{eff}}(\boldsymbol{x}''_\perp)\mathrm{d}r''_\perp\right]\mathrm{d}v_\perp \tag{24b}$$

$$K_{\mathrm{p}\to\mathrm{b}}(\boldsymbol{x}_{\perp\mathrm{b}},\boldsymbol{x}'_\perp)=\int_0^\infty \frac{v_\perp}{r'_\perp}\cos\theta\Phi_{\perp\mathrm{i}}(\boldsymbol{x}'_\perp,\boldsymbol{v}_\perp)\times\exp\left[-\frac{1}{v_\perp}\int_0^{r'_\perp}\nu_{\mathrm{eff}}(\boldsymbol{x}''_\perp)\mathrm{d}r''_\perp\right]\mathrm{d}v_\perp \tag{24c}$$

$$K_{\mathrm{b}\to\mathrm{b}}(\boldsymbol{x}_{\perp\mathrm{b}},\boldsymbol{x}'_{\perp\mathrm{b}})=\int_0^\infty \frac{v_\perp^2}{r'_\perp}\cos\theta\cos\theta'\chi_{\perp\mathrm{in}}(\boldsymbol{x}'_\mathrm{b},\boldsymbol{v})\times\exp\left[-\frac{1}{v_\perp}\int_0^{r'_\perp}\nu_{\mathrm{eff}}(\boldsymbol{x}''_\perp)\mathrm{d}r''_\perp\right]\mathrm{d}v_\perp, \tag{24d}$$

where $\Phi_{\perp\mathrm{i}}(\boldsymbol{x}_\perp,\boldsymbol{v}_\perp)=\int\Phi_\mathrm{i}(\boldsymbol{x}_\perp,\boldsymbol{v})\mathrm{d}v_\parallel=m_\mathrm{i}/(2\pi T_\mathrm{i})\exp\left[-m_\mathrm{i}v_\perp^2/(2T_\mathrm{i})\right]$, $\chi_{\perp\mathrm{in}}(\boldsymbol{x}_\perp,\boldsymbol{v}_\perp)=\int\chi_{\mathrm{in}}(\boldsymbol{x}_\perp,\boldsymbol{v})\mathrm{d}v_\parallel=3m_\mathrm{i}^2/(4\pi T_\mathrm{i}^2)v_\perp\cos\theta\ \exp\left[-m_\mathrm{i}v_\perp^2/(4T_\mathrm{i})\right]\mathcal{K}_0[m_\mathrm{i}v_\perp^2/(4T_\mathrm{i})]$, and $\mathcal{K}_0(x)$ is the modified Bessel function of the second kind.

The four kernels, equations (24), depict the four different possible paths for neutral particles: originating from within the plasma or from the boundary, and arriving at a position in the plasma or on the boundary. All kernels include an exponentially decaying term, to take into account the loss of neutrals between the origin and arrival positions due to ionization and charge-exchange collisions. Furthermore, we note that neutrals that are emitted in the plasma region originate from a source proportional to $\Phi_{\perp\mathrm{i}}$ (see $K_{\mathrm{p}\to\mathrm{p}}$ and $K_{\mathrm{p}\to\mathrm{b}}$), while neutrals are emitted at the boundary with a source proportional to $\chi_{\perp\mathrm{in}}v_\perp\cos\theta'$ (see $K_{\mathrm{b}\to\mathrm{p}}$ and $K_{\mathrm{b}\to\mathrm{b}}$). Since Γ_{out} describes the perpendicular outflow into the boundary, the kernels $K_{\mathrm{p}\to\mathrm{b}}$ and $K_{\mathrm{b}\to\mathrm{b}}$ include a $v_\perp\cos\theta$ term.

The neutral density and the neutral outflow caused by volumetric recombination are evaluated using kernels $K_{\mathrm{p}\to\mathrm{p}}$ and $K_{\mathrm{p}\to\mathrm{b}}$ resulting in $n_{\mathrm{n,rec}}(\boldsymbol{x}_\perp)=\int_D n_\mathrm{i}(\boldsymbol{x}'_\perp)\nu_{\mathrm{rec}}(\boldsymbol{x}'_\perp)K_{\mathrm{p}\to\mathrm{p}}(\boldsymbol{x}_\perp,\boldsymbol{x}'_\perp)\mathrm{d}A'$, and $\Gamma_{\mathrm{out,rec}}(\boldsymbol{x}_{\perp\mathrm{b}})=\int_D n_\mathrm{i}(\boldsymbol{x}'_\perp)\nu_{\mathrm{rec}}(\boldsymbol{x}'_\perp)K_{\mathrm{p}\to\mathrm{b}}(\boldsymbol{x}_{\perp\mathrm{b}},\boldsymbol{x}'_\perp)\mathrm{d}A'$. We remark that the kernel functions, $K_{\mathrm{p}\to\mathrm{p}}$, $K_{\mathrm{b}\to\mathrm{p}}$, $K_{\mathrm{p}\to\mathrm{b}}$, and $K_{\mathrm{b}\to\mathrm{b}}$, do neither depend on $f_\mathrm{n}(\boldsymbol{x}_\perp,\boldsymbol{v})$, nor on any of its moments. They can be evaluated once the problem geometry and the plasma properties are known.

Having solved equation (21), therefore once $n_\mathrm{n}(\boldsymbol{x}_\perp)$ is known, the distribution function of the neutral atoms, $f_\mathrm{n}(\boldsymbol{x}_\perp,\boldsymbol{v})$, can be readily evaluated by using equation (14). At that point, the moments of $f_\mathrm{n}(\boldsymbol{x}_\perp,\boldsymbol{v})$ that are needed in the neutral-plasma interaction terms presented in the drift-reduced Braginskii equations, equations (9), such as the fluid parallel neutral velocity, $v_\mathrm{n}(\boldsymbol{x}_\perp)$, and the neutral temperature, $T_\mathrm{n}(\boldsymbol{x}_\perp)$, can be computed without difficulties. The numerical discretization and the convergence properties of the neutral model are described in appendix.

4. First plasma turbulence simulations with self-consistent neutral dynamics

The neutral model derived in this paper has been used to perform the first simulations of SOL plasma turbulence that include self-consistently the neutral dynamics. For this purpose, the GBS code has been extended by implementing the neutral model and the plasma-neutral interaction terms in the fluid equations. We compare here a low plasma density simulation, where the recycled neutrals are mostly ionized in the tokamak core, and therefore the source of SOL plasma is mainly due to the plasma outflow from the core (this simulation features the sheath limited regime), with a high plasma density simulation, where SOL plasma is coming partly from the core and partly from the recycling process occurring inside the SOL (several features of the so-called conduction limited regime are displayed by this simulation). Both simulations consider a limited SOL geometry, with a toroidal limiter on the high field equatorial midplane, $R/\rho_{\mathrm{s}0}=500$, $m_\mathrm{i}/m_\mathrm{e}=400$, $2\pi a=800\rho_{\mathrm{s}0}$, a being the minor radius, and $T_{\mathrm{e}0}=10$ eV. Furthermore, in the low plasma density simulation, we impose $n_0=5{\cdot}10^{18}$ m^{-3}, the value of the density at the LCFS, and $\tilde{\nu}=Rm_\mathrm{e}/(1.96c_{\mathrm{s}0}m_\mathrm{i}\tau_\mathrm{e})=0.02$, the resistivity normalized to $R/c_{\mathrm{s}0}$. As a consequence, the dimensionless parallel electron heat conductivity is $\tilde{\kappa}_{\parallel\mathrm{e}}=3.16\times 2T_{\mathrm{e}0}\tau_\mathrm{e}/(3m_\mathrm{e}c_{\mathrm{s}0}R)=56.0$, the dimensionless parallel ion heat conductivity is $\tilde{\kappa}_{\parallel\mathrm{i}}=3.9\times 2T_{\mathrm{i}0}\tau_\mathrm{i}/(3m_\mathrm{i}c_{\mathrm{s}0}R)=1.6$, and the dimensionless

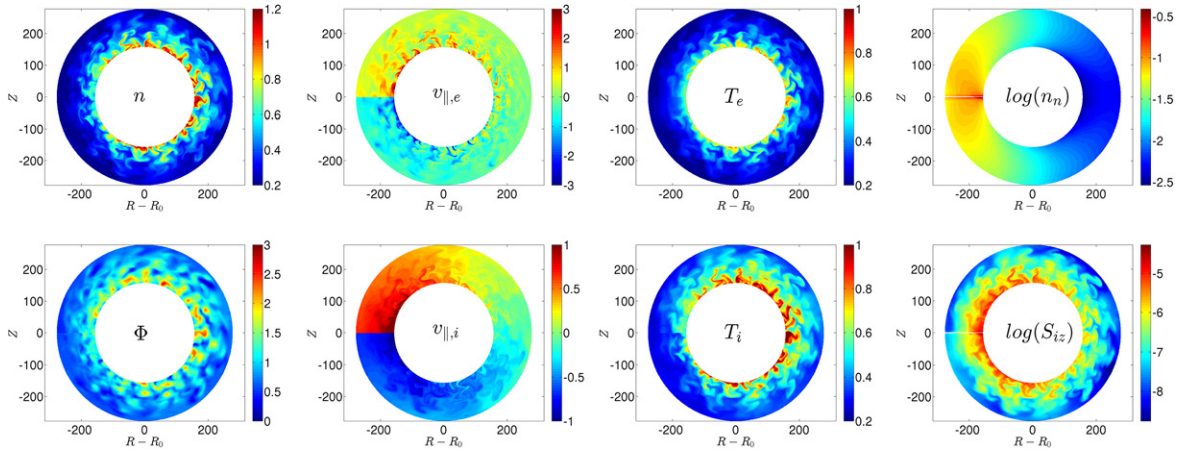

Figure 2. Snapshots on a poloidal cross-section of plasma density, electric potential, ion and electron parallel velocities, electron and ion temperatures, neutral density, and the ionization source term, $S_{\rm iz}$, for the low-density simulation, $n_0 = 5 \cdot 10^{18}\,{\rm m}^{-3}$.

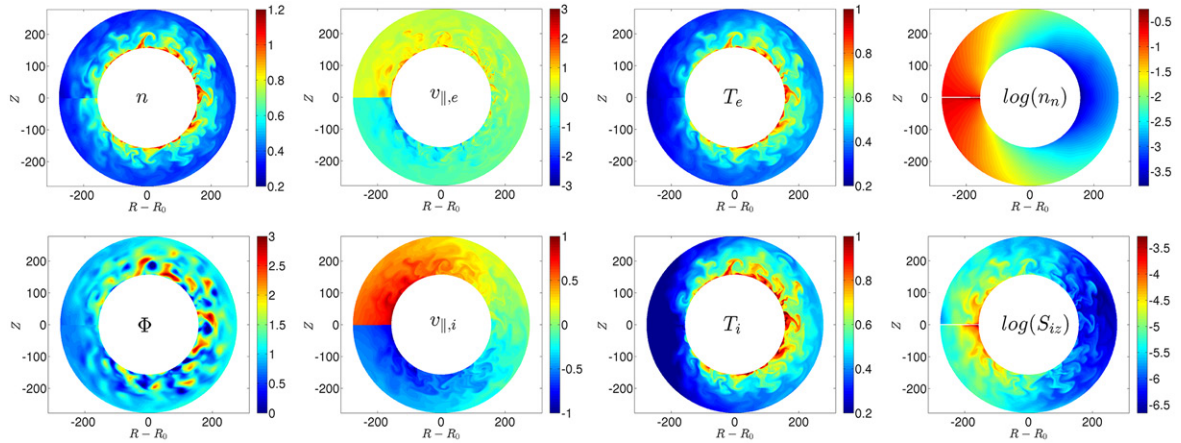

Figure 3. Snapshots on a poloidal cross-section of plasma density, electric potential, ion and electron parallel velocities, electron and ion temperatures, neutral density, and the ionization source term, $S_{\rm iz}$, for the high-density simulation, $n_0 = 5 \cdot 10^{19}\,{\rm m}^{-3}$.

electron viscosity coefficient is $\tilde{\eta}_{\rm e0} = 0.73 T_{\rm e0}\tau_{\rm e}/(m_{\rm e}Rc_{\rm s0}) = 20.0$. In the high plasma density simulation, $n_0 = 5 \cdot 10^{19}\,{\rm m}^{-3}$, $\tilde{\nu} = 0.2$, $\tilde{\kappa}_{\parallel {\rm e}} = 5.6$, $\tilde{\kappa}_{\parallel {\rm i}} = 0.16$, and $\tilde{\eta}_{\rm e0} = 2.0$ are used. The computational domain extends from $r_{\rm min} = 0$ to $r_{\rm max} = 150\rho_{\rm s0}$. The source terms $S_{\rm n}$, $S_{T_{\rm i}}$, and $S_{T_{\rm e}}$ in equations (9) are constant in time, poloidally uniform, and radially Gaussian around $r_{\rm s} = 30\rho_{\rm s0}$, that we interpret as the radial position of the LCFS. Quantities displayed in the figures are normalized to n_0, $c_{\rm s0}$, and $T_{\rm e0}$.

In figures 2 and 3 typical snapshots of plasma density, parallel electron and ion velocities, electron and ion temperatures, electrostatic potential, neutral density, and ionization source, $S_{\rm iz} = n_{\rm n}\nu_{\rm iz}$, are shown on a poloidal cross-section. They show fully developed turbulence during the saturated state of the two simulations.

The poloidal dependence of the relevant plasma quantities (plasma density, electron and ion parallel velocities, electron and ion temperatures, electrostatic potential, neutral density, and $S_{\rm iz}$) for the low- and high-density simulations are shown in figure 4. The displayed profiles are averaged over a time window of 20 $R/c_{\rm s0}$, over the full toroidal angle, and over a radial region extending for 20 $\rho_{\rm s0}$, centered at a distance of 30 $\rho_{\rm s0}$ from the separatrix.

We point out a few interesting differences between the high- and low-density simulations. The poloidal density profile in the high-density simulation is flatter than in the low-density simulation. This is due to the fact that the plasma source due to the ionizations occurring close to the limiter inside the SOL is much higher in the high-density simulation, preventing the plasma density to drop when approaching the sheaths. The parallel velocity profiles (which are expected to be approximately linear if the plasma source is poloidally constant) are somewhat flatter close to the limiter in the high-density scenario; however, the flattening is not particularly significant, because a relatively large fraction of the plasma density source is still due to the poloidally constant outflow of particles from the core. Furthermore, both electron and ion temperature poloidal gradients increase in the high-density scenario, which is expected while going towards the conduction limited regime. The mechanisms that lead to this temperature drop include the reduced parallel heat conductivity (due to lower temperature and higher density), and the direct energy loss due to ionizations (see, e.g. [18]). To verify that these are the acting mechanism behind the temperature drop in the high-density scenario, the balance of

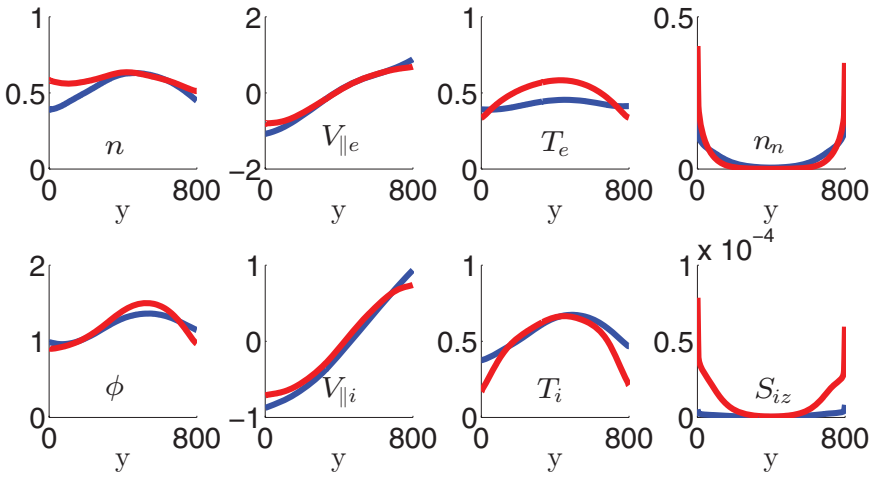

Figure 4. Time-averaged poloidal profiles of n, Φ, $V_{\|e}$, $V_{\|i}$, T_e, T_i, n_n, and S_{iz} for the low (blue) and high (red) plasma density scenario.

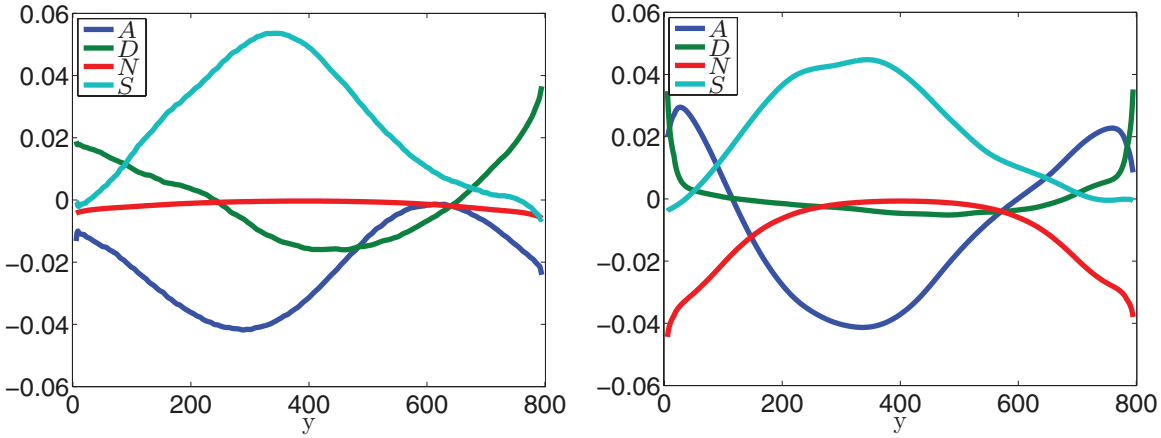

Figure 5. Time-averaged poloidal balance of the electron temperature equation for the low (left) and high (right) density case. The shown terms are the parallel advection, A, the parallel diffusion, D, the contribution of the neutral interaction, N, and the sources in the electron temperature equation, S.

the electron temperature equation (9*e*), in quasi steady state is shown in figure 5. The terms on the right hand side of equation (9*e*) are toroidally, radially, and time averaged, in the same way as the poloidal profiles in figure 4. The terms are arranged into four groups, namely, the parallel advection term, $A = -v_{\|e}\nabla_\| T_e + 2T_e/(3n)[0.71/e\nabla_\| j_\| - n\nabla_\| v_{\|e}]$, the parallel diffusion term, $D = \mathcal{D}^\|_{T_e}(T_e)$, the plasma-neutral interaction term, $N = n_n\nu_{iz}/n[-2E_{iz}/3 - T_e + m_e v_{\|e}(v_{\|e} - 4v_{\|n}/3)] - n_n\nu_{en}m_e 2v_{\|e}/(3n)(v_{\|n} - v_{\|e})$, and the source term, $S = -1/B[\phi, T_e] + 4T_e/(3eB)[T_e C(n)/n + 7C(T_e)/2 - eC(\phi)] + \mathcal{D}_{T_e}(T_e) + S_{T_e}$, which includes the divergence of the flow due to the $\boldsymbol{E}\times\boldsymbol{B}$ and curvature drifts. It has been verified that the sum of the four terms converges towards zero as we increase the time-span over which the average is evaluated. From figure 5, it is apparent that both before mentioned mechanisms are important for the steepening of the electron temperature gradient. While the source term, S, has almost the same shape in the two scenarios, the plasma-neutral interaction term, N, is clearly important only in the high-density simulation (the most important contribution to N is due to the ionization process, $-2n_n\nu_{iz}E_{iz}/(3n)$). The effect of N is to decrease the electron temperature close to the limiter. Furthermore, the parallel diffusion term, D, has a larger impact on the low-density simulation, where it flattens the temperature profile. In the low-density simulation, the importance of the parallel diffusion term arises from the high parallel electron conductivity, inversely proportional to the plasma density. In the-high density simulation, the parallel diffusion term plays a significant role only in proximity of the limiter.

5. Conclusions and outlook

In this paper we have presented a first-principles self-consistent model suitable to simulate the coupled plasma turbulent and neutral dynamics in the tokamak SOL. The model assumes high plasma collisionality, $\omega_c\tau \gg 1$, drift ordering, $\mathrm{d}/\mathrm{d}t \ll \omega_{ci}$, adiabatic neutrals, $\tau_n < \tau_{turb}$, and elongated turbulent plasma structures, $k_\|\lambda_{mfp,n} \ll 1$. The plasma is modeled by the drift-reduced two-fluid Braginskii equations, equations (9), and the neutral physics is described by a kinetic equation with Krook operators for ionization, recombination, and charge-exchange processes, equation (1). The neutral kinetic equation is solved in the adiabatic limit using decoupled poloidal planes and a short cycle scheme. The kinetic equation is hereby reduced to a linear integral equation for the neutral density, equation (21).

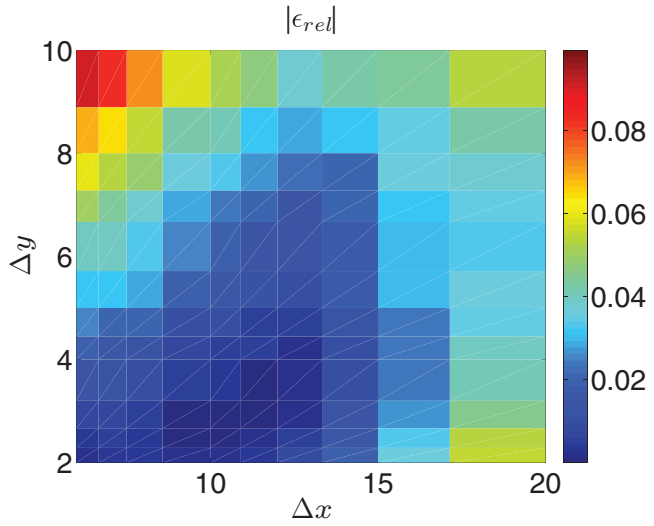

Figure A1. Relative error of the neutral particle conservation, ϵ_{rel}, as a function of the grid spacing in the radial, Δx, and poloidal, Δy, directions. The low density scenario, $n_0 = 5 \cdot 10^{18}$ m^{-3}, which is presented in section 4, is considered.

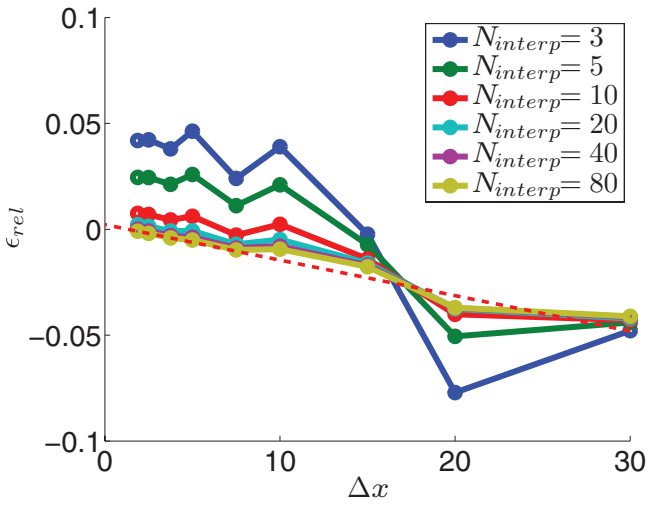

Figure A2. Convergence of the numerical error depending on the grid size and the number of interpolation points. In particular, we have considered $\Delta x = [30, 20, 15, 10, 7.5, 5, 3.75, 2.5, 1.875]$, $\Delta y = \Delta x/2.5$, and $N_{\text{interp}} = [3, 5, 10, 20, 40, 80]$. The red dashed line is the extrapolation of ϵ_{rel} to $\Delta x = 0$ for the $N_{\text{interp}} = 80$ case. The last three points, with the smallest Δx, have been considered.

Obtaining the neutral density enables the straightforward computation of the neutral distribution function, f_{n}, by evaluating equation (14), and any of its higher order moments, as needed in the plasma equations.

We have performed the first simulations with the newly developed model and promising initial results, showing the expected changes in the plasma profiles, have been briefly discussed. As a matter of fact, we have developed a new tool to study the effect of the neutral dynamics on SOL turbulence, which enables us to investigate a rich variety of SOL physics phenomena, while being conceptually simple and numerically affordable. We intend to apply it to investigate the transition between the different SOL regimes, focusing

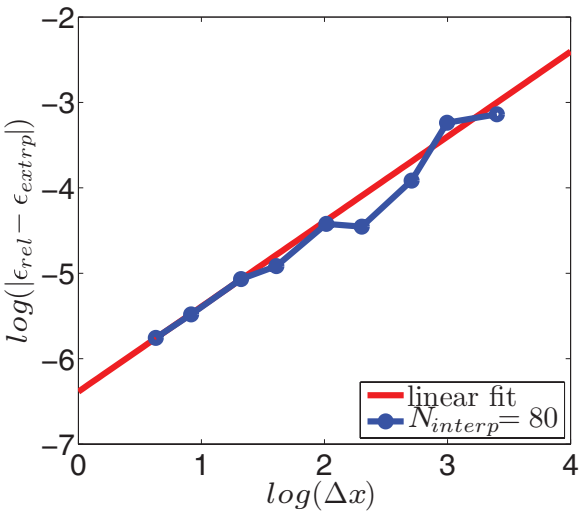

Figure A3. Log–log plot of the numerical error, ϵ_{rel}, as a function of the spatial discretization, Δx ($\Delta y = \Delta x/2.5$), for the case $N_{\text{interp}} = 80$, including a linear fit ($\log(|\epsilon_{\text{rel}} - \epsilon_{\text{extrp}}|) = 0.995 \log(\Delta x) - 6.39$, using the three points with the smallest Δx for the fitting procedure) to demonstrate linear order of convergence.

first on the transition between the sheath and the conduction limited regimes, and to study the effect of the neutrals on SOL turbulent properties, in particular the linear properties of the unstable modes, their saturation, and, ultimately, their impact on the SOL width.

Acknowledgments

The authors acknowledge useful discussions with D. Reiter and M. Wischmeier. Part of the simulations presented herein were carried out using the HELIOS supercomputer system at Computational Simulation Centre of International Fusion Energy Research Centre (IFERC-CSC), Aomori, Japan, under the Broader Approach collaboration between Euratom and Japan, implemented by Fusion for Energy and JAEA; and part were carried out at the Swiss National Supercomputing Centre (CSCS) under Project ID s549. This work has been carried out within the framework of the EUROfusion Consortium and has received funding from the Euratom research and training programme 2014–2018 under grant agreement No 633053. The views and opinions expressed herein do not necessarily reflect those of the European Commission.

Appendix. Numerical solution and convergence tests

In the following we introduce the discretization of equation (21) necessary for its numerical solution and show some tests to illustrate the numerical convergence properties of our model. The spatial discretization for the neutral equation can be set independently of the grid on which the plasma quantities are evolved. If the two spatial discretizations do not match, a linear two-dimensional interpolation routine is used to port the plasma and neutral fields from one grid to the other. We remark that the

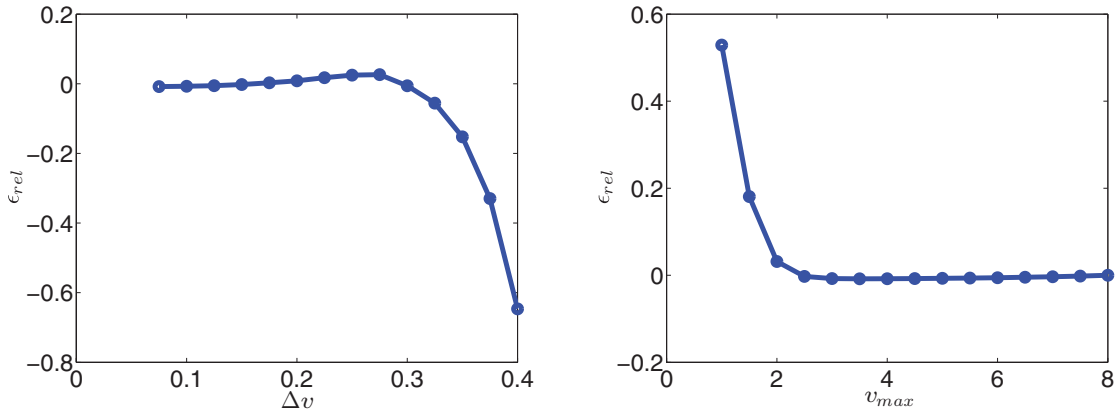

Figure A4. Relative error of particle conservation, $\epsilon_{\rm rel}$, as a function of the velocity discretization. (Both cases use $\Delta x = 2.5\Delta y = 7.5$, and $N_{\rm interp} = 20$.) (a) Convergence is observed for $\Delta v \lesssim 0.25 c_{\rm s0}$ (having fixed $v_{\rm max} = 5.0 c_{\rm s0}$). (b) Convergence is observed for $v_{\rm max} \gtrsim 2.5 c_{\rm s0}$ (having fixed $\Delta v = 0.1 c_{\rm s0}$).

use of any grid to solve equation (21), including unstructured meshes, does not present any conceptual difficulty.

On a discretized spatial grid, equations (21) and (22) assume the form

$$n_{\rm n}^i = \sum_j K_{\rm p\to p}^{i,j} \nu_{\rm cx}^j n_{\rm n}^j + \sum_j K_{\rm b\to p}^{i,j} \Gamma_{\rm out}^j + n_{\rm n,rec}^i \tag{A.1}$$

and

$$\Gamma_{\rm out}^i = \sum_j K_{\rm p\to b}^{i,j} \nu_{\rm cx}^j n_{\rm n}^j + \sum_j K_{\rm b\to b}^{i,j} \Gamma_{\rm out}^j + \Gamma_{\rm out,rec}^i + \Gamma_{\rm out,i}^i \tag{A.2}$$

where i and j are grid cell indices (the i-th grid cell is centered around $\boldsymbol{x}_\perp^i$ and has an area ΔA^i), and

$$K_{\rm p\to p}^{i,j} = \frac{\Delta A^j}{r^{ij}} \int_0^\infty \Phi_{\perp \rm i}(\boldsymbol{x}_\perp^j, v_\perp \hat{\boldsymbol{r}}^{ij}) \times \exp\left[-\frac{1}{v_\perp}\int_0^{r^{ij}} \nu_{\rm eff}(\boldsymbol{x}_\perp^j + r'\hat{\boldsymbol{r}}^{ij}) {\rm d}r'\right] {\rm d}v_\perp \tag{A.3}$$

with $\boldsymbol{r}^{ij} = \boldsymbol{x}_\perp^i - \boldsymbol{x}_\perp^j$, and $\hat{\boldsymbol{r}}^{ij} = \boldsymbol{r}^{ij}/r^{ij}$. Equivalent expressions apply to the other kernels.

In equation (A.3), the velocity integral is discretized in equidistant velocity intervals of size Δv, centered around $(i_v + 1/2)\Delta v$, usually up to $v_{\rm max} = 5 c_{\rm s0}$, and computed by using the rectangle rule. On the other hand, the line integral between $\boldsymbol{x}_\perp^i$ and $\boldsymbol{x}_\perp^j$, $\int_0^{r^{ij}} \nu_{\rm eff}(\boldsymbol{x}_\perp^j + r'\hat{\boldsymbol{r}}^{ij}){\rm d}r'$, is equidistantly discretized into $N_{\rm interp} + 1$ intervals, and integrated using the trapezoidal rule. The values of $\nu_{\rm eff}(\boldsymbol{x}_\perp^j + r'\hat{\boldsymbol{r}}^{ij})$ required for the evaluation of the integral are obtained by using linear interpolation from the grid values.

Equations (A.1) and (A.2) are a system of linear equations that can be recast in matrix form

$$\begin{bmatrix} n_{\rm n} \\ \Gamma_{\rm out} \end{bmatrix} = \begin{bmatrix} K_{\rm p\to p} & K_{\rm b\to p} \\ K_{\rm p\to b} & K_{\rm b\to b} \end{bmatrix} \cdot \begin{bmatrix} n_{\rm n} \\ \Gamma_{\rm out} \end{bmatrix} + \begin{bmatrix} n_{\rm n,rec} \\ \Gamma_{\rm out,rec} + \Gamma_{\rm out,i} \end{bmatrix} \tag{A.4}$$

and that can be solved with standard full matrix solvers. We note that, in the simulations presented in this paper, the matrix is typically filled by one third, since not every pair of grid cells is optically connected. The fraction of non-zero entries decreases at larger system size. As a matter of fact, entries of pairs that are separated by several $\lambda_{\rm mfp,n}$ could be neglected, making the fraction of non-zero elements even smaller. This possibility, as well as the related use of sparse matrix solvers, will be explored in a future work.

Since the solution of equation (A.1) is particularly expensive, we use a short cycling scheme, as described in [5] and used, e.g. in [11]. More precisely, to apply the short cycle scheme, we recalculate the neutral density every time interval, $\Delta t_{\rm n}$, where $\Delta t_{\rm n}$ is comparable to the turbulent timescales and longer than the typical time step used to advance numerically the drift-reduced Braginskii equations. However, the interaction terms in the plasma equations, equations (9) (e.g. $n_{\rm n}\nu_{\rm iz} = n_{\rm n} n \langle v_{\rm e}\sigma_{\rm iz}\rangle$) are recalculated at every time-step, taking into account the changing plasma quantities (e.g. n), and the change in reaction rates (e.g. $\langle v_{\rm e}\sigma_{\rm iz}\rangle$), which depend on the plasma temperatures.

To illustrate the numerical convergence properties, we consider the relative error in the conservation of neutral particles, defined as

$$\epsilon_{\rm rel} = \frac{N_{\rm in} - N_{\rm out}}{N_{\rm in}} \tag{A.5}$$

where $N_{\rm in} = \sum_i \Gamma_{\rm out,i}^i \Delta a_{\rm b}^i + \sum_i n_{\rm i}^i \nu_{\rm rec}^i \Delta A^i$ is the number of neutrals that are created in a time unit due to ion recycling and recombination, and $N_{\rm out} = \sum_i n_{\rm n}^i \nu_{\rm iz}^i \Delta A^i + \sum_i \Gamma_{\rm out,core}^i \Delta a_{\rm b}^i$ is the number of neutrals lost from the system in a time unit due to ionization and outflow to the core plasma. For the numerical tests in the remainder of this section we consider the low-density plasma scenario described in detail in section 4.

We carry out three convergence tests. We first study the convergence of the numerical solution with the spatial discretization. We use the radial distance from the LCFS, r, and the poloidal angle, ϑ, as coordinates in the poloidal plane, which we discretize on a grid with equidistant points separated by the normalized distances $\Delta x = \Delta r/\rho_{\rm s0}$ in the radial direction and $\Delta y = a/\rho_{\rm s0}\Delta\vartheta$ in the poloidal direction (a is the minor

plasma radius). Figure A1 shows a convergence study on the spatial discretization. The best converged results are obtained for $2 \lesssim \Delta x/\Delta y \lesssim 4$. (The variation of the neutral quantities is stronger in the poloidal than in the radial direction.) Then, we perform a scan of solutions of equation (A.4) by varying the grid spacing and N_{interp} independently. The results are presented in figure A2. For small N_{interp}, the error does not converge to zero, but towards a finite value that is determined by the error associated with the discretization of the line integral between $\boldsymbol{x}_\perp$ and $\boldsymbol{x}'_\perp$. This error decreases with increasing N_{interp} as it is shown in figure A2. To calculate the order of convergence, we extrapolate the error of the $N_{\text{interp}} = 80$ curve to $\Delta x = 0$, to obtain $\epsilon_{\text{extrp}} = \epsilon(\Delta x = 0)$, where ϵ_{extrp} includes the numerical error from the discretization of the line integral between $\boldsymbol{x}_\perp$ and $\boldsymbol{x}'_\perp$, as well as the numerical errors from the velocity space discretization. Figure A3 shows the error due to the spatial grid discretization, $\epsilon_{\text{rel}} - \epsilon_{\text{extrp}}$, and reveals that the numerical algorithm has a linear convergence with respect to the grid spacing. Typically, $\Delta x \simeq 2.5$, $\Delta y \simeq 7.5$, and $N_{\text{interp}} = 20$ are used in our simulations.

The second test investigates the convergence with respect to the discretization of the velocity integral inside the kernel functions. Figure A4(a) shows the convergence with Δv for fixed $v_{\max} = 5.0 c_{s0}$, while figure A4(b) shows the convergence with $v_{\max}$ for fixed $\Delta v = 0.1 c_{s0}$. Both figures show convergence towards a finite value of ϵ_{err}, which is the error due to the spatial discretization. Typically, $\Delta v = 0.1 c_{s0}$ and $v_{\max} = 5 c_{s0}$ are used in our simulations.

For the third convergence test, we performed a set of simulations of SOL plasma dynamics by solving the drift-reduced Braginskii equations with the self-consistent neutral module. We set $\Delta t_{\text{n}} = 0.01$, 0.05, 0.2, 1, and 5 R/c_{s0}. The results of all simulations show no significant nor systematic differences in the averaged plasma quantities. In fact, the neutral density is approximatively constant throughout a simulation. The time dependence of the collisionalities is due mainly to the evolution of the plasma density and temperatures, while the neutral density strongly influences the spatial dependence of the collision rates.

References

[1] Reiter D. *et al* 2002 EIRENE—a monte carlo linear transport solver available on the internet at www.eirene.de

[2] Stotler D. and Karney C. 1994 Neutral gas transport modeling with DEGAS 2 *Contrib. Plasma Phys.* **34** 392–7

[3] Cupini E., De Matteis A. and Simonini R. 1983 *NIMBUS-Monte Carlo Simulation of Neutral Particle Transport in Fusion Devices* (Brussels: Commission of the European Communities) EUR XII-324/9

[4] Bufferand H. *et al* 2013 Near wall plasma simulation using penalization technique with the transport code SOLEDGE2D-EIRENE *J. Nucl. Mater.* **438** S445–8

[5] Reiter D. 1992 Progress in two-dimensional plasma edge modelling *J. Nucl. Mater.* **196–8** 80–9

[6] Schneider R., Reiter D., Zehrfeld H.P., Braams B., Baelmans M., Geiger J., Kastelewicz H., Neuhauser J. and Wunderlich R. 1992 B2-EIRENE simulation of ASDEX and ASDEX-upgrade scrape-off layer plasmas *J. Nucl. Mater.* **196–8** 810–5

[7] Reiter D., Baelmans M. and Börner P. 2005 The EIRENE and B2-EIRENE codes *Fusion Sci. Technol.* **47** 172–86

[8] Feng Y., Sardei F., Kisslinger J., Grigull P., McCormick K. and Reiter D. 2004 3D edge modeling and island divertor physics *Contrib. Plasma Phys.* **44** 57–69

[9] Rognlien T.D., Milovich J.L., Rensink M.E. and Porter G.D. 1992 A fully implicit, time dependent 2D fluid code for modeling tokamak edge plasmas *J. Nucl. Mater.* **196–8** 347–51

[10] Kukushkin A.S., Pacher H.D., Kotov V., Pacher G.W. and Reiter D. 2011 Finalizing the ITER divertor design: the key role of SOLPS modeling *Fusion Eng. Des.* **86** 2865–73

[11] Marandet Y., Tamain P., Futtersack R., Ghendrih Ph., Bufferand H., Genesio P. and Mekkaoui A. 2013 Influence of neutral particles on scrape-off layer turbulence with application to the interpretation of fast camera data *J. Nucl. Mater.* **438** 518–21

[12] Bisai N., Jha R. and Kaw P.K. 2015 Role of neutral gas in scrape-off layer tokamak plasma *Phys. Plasmas* **22** 022517

[13] Mekkaoui S., Dudson B., Reiter D., Kotov V. and Boerner P. 2014 Self-consistent turbulence-recycling modeling in the lapd device [abstract] *21st Int. Conf. on Plasma Surface Interactions (Ongaku-do, Kanazawa Ishikawa, Japan, 26–30 May 2014)* P3–095 http://psi2014.nifs.ac.jp

[14] Braginskii S.I. 1965 Transport processes in a plasma *Rev. Plasma Phys.* **1** 205

[15] Ricci P., Halpern F.D., Jolliet S., Loizu J., Mosetto A., Fasoli A., Furno I. and Theiler C. 2012 Simulation of plasma turbulence in scrape-off layer conditions: the GBS code, simulation results and code validation *Plasma Phys. Control. Fusion* **54** 124047

[16] Loizu J., Ricci P., Halpern F.D. and Jolliet S. 2012 Boundary conditions for plasma fluid models at the magnetic presheath entrance *Phys. Plasmas* **19** 122307

[17] Halpern F.D., Jolliet S., Loizu J., Mosetto A. and Ricci P. 2013 Ideal ballooning modes in the tokamak scrape-off layer *Phys. Plasmas* **20** 052306

[18] Stangeby P. 2000 *The Plasma Boundary of Magnetic Fusion Devices* (Bristol: IOP)

[19] Summers H.P., Dickson W.J., O'Mullane M.G., Badnell N.R., Whiteford A.D., Brooks D.H., Lang J., Loch S.D. and Griffin D.C. 2006 Ionization state, excited populations and emission of impurities in dynamic finite density plasmas: I. The generalized collisional–radiative model for light elements *Plasma Phys. Control. Fusion* **48** 263–93

[20] Knudsen M. 1916 Das cosinusgesetz in der kinetischen gastheorie *Annal. Phys.* **353** 1113–21

[21] Helander P., Krasheninnikov S.I. and Catto P.J. 1994 Fluid equations for a partially ionized plasma *Phys. Plasmas* **1** 3174

[22] Zeiler A., Drake J.F. and Rogers B. 1997 Nonlinear reduced Braginskii equations with ion thermal dynamics in toroidal plasma *Phys. Plasmas* **4** 2134

[23] Ricci P. and Rogers B.N. 2013 Plasma turbulence in the scrape-off layer of tokamak devices *Phys. Plasmas* **20** 010702

[24] Mosetto A., Halpern F.D., Jolliet S., Loizu J. and Ricci P. 2013 Turbulent regimes in the tokamak scrape-off layer *Phys. Plasmas* **20** 092308

[25] Loizu J., Ricci P., Halpern F.D., Jolliet S. and Mosetto A. 2014 Intrinsic toroidal rotation in the scrape-off layer of tokamaks *Phys. Plasmas* **21** 062309

[26] Halpern F.D., Ricci P., Jolliet S., Loizu J. and Mosetto A. 2014 Theory of the scrape-off layer width in inner-wall limited tokamak plasmas *Nucl. Fusion* **54** 043003

[27] Loizu J., Ricci P., Halpern F.D., Jolliet S. and Mosetto A. 2013 On the electrostatic potential in the scrape-off layer of magnetic confinement devices *Plasma Phys. Control. Fusion* **55** 124019

[28] Marandet Y. *et al* 2011 Transport of neutral particles in turbulent scrape-off layer plasmas *Nucl. Fusion* **51** 083035